Exact shearing box solutions of MHD flows with resistivity, viscosity and cooling

Pierre Lesaffre[1][*] and Steven A. Balbus[1,2]
[1] *Laboratoire de Radioastronomie, 24 rue Lhomond, 75231 PARIS Cedex 05, France*
[2] *Adjunct Professor, Dept. of Astronomy, University of Virginia, Charlotesville V1 22903*

ABSTRACT

Axisymmetric incompressible modes of the magneto-rotational instability (MRI) with a vertical wavenumber are exact solutions of the non-linear local equations of motion for a disk (shearing box). They are referred to as "channel solutions". Here, we generalize a class of these solutions to include energy losses, viscous, and resistive effects. In the limit of zero shear, we recover the result that torsional Alfvén waves are exact solutions of the non-linear equations. Our method allows the extension of these solutions into the dissipative regime.

These new solutions serve as benchmarks for simulations including dissipation and energy loss, and to calibrate numerical viscosity and resistivity in the Zeus3D code. We quantify the anisotropy of numerical dissipation and compute its scaling with time and space resolution. We find a strong dependence of the dissipation on the mean magnetic field that may affect the saturation state of the MRI as computed with Zeus3D. It is also shown that elongated grid cells generally preclude isotropic dissipation and that a Courant time step smaller than that which is commonly used should be taken to avoid spurious anti-diffusion of magnetic field.

Key words: analytic solutions – time-dependent – MHD – cooling – resistivity – viscosity

1 INTRODUCTION

The magneto-rotational instability (MRI) (Balbus & Hawley 1991), is generally regarded as the best candidate for explaining the "anomalous viscosity" that transports angular momentum through accretion disks. The first two-dimensional numerical studies of the MRI (Hawley & Balbus 1992) revealed a surprise: the flow broke along the vertical axis into two distinct and regular sheets, which appeared as channels when visualized in a meridional plane. In this plane, which projects out azimuthal motion, the perturbed velocities are nearly radial, one flowing inward, the other outward. This pattern was given the name of *channel solution*. It is a recurring feature of more general three-dimensional global numerical simulations of the MRI, appearing intermittently. Indeed the most unstable linear modes of the MRI are modes with a vertical wavenumber, which are, in effect, channel solutions.

Goodman & Xu (1994) showed that these modes could be destroyed by three-dimensional parasitic instabilities, notably the magnetic Kelvin-Helmoltz (KH) instability. Such studies are important for the light they may shed on the process of the saturation of MRI turbulence. Resistivity and viscosity are also key to the saturation of the MRI, as channel flows break down and fields reconnect. As the power of computers increases, more of these important microphysical processes are being included in the simulations. On the other hand, as the complexity of codes increases, fewer benchmarks are available to check and calibrate the implementation of numerical methods. It is this issue that motivates this paper.

One of the key insights of Goodman & Xu (1994) was to note that the linear modes of the MRI are *exact* solutions of the non-linear local equations of incompressible magnetohydrodynamics (MHD). This is also seen in non-linear circularly polarised

---

[*] Email: pierre.lesaffre@lra.ens.fr

torsional Alfvén waves, whose linear modes exactly satisfy the non-linear MHD equations for a polytropic (or incompressible) gas. In this paper, we will establish a connection between these two types of solution.

It is the purpose of this paper to extend the Goodman-Xu solutions to include viscosity and resistivity. We are also able to find solutions that include a net heating or cooling term, provided that such gains/losses are linear in the temperature. We first compute the linear MRI modes with a vertical wavenumber in the shearing box regime with viscous and resistive terms included. We show that the only remaining non-linear term is the total pressure gradient (magnetic plus kinetic), and we establish a condition for it to vanish (Section 2). In the next two sections we investigate less general cases without viscosity (Section 3) or without shear (Section 4), for which we can give extended families of analytic solutions. In Section 5 we provide methods for finding isolated solutions under more general assumptions. We then present two applications of our results: in Section 6 we benchmark a new version of the Zeus3D code with a conservative scheme for total energy; in Section 7 we use our solutions to compute the numerical resistivity and the numerical viscosity in the Zeus3D code. We discuss our results and conclude in Sections 8 and 9.

2   GENERAL METHOD

2.1   Shearing sheet

The shearing sheet system results from a local first order expansion of the dynamical equations of motion, with the inverse radius serving as the small parameter. This approach dates back to a celestial mechanics calculation of Hill (1878). The frame of reference rotates at circular angular velocity Ω. Radial, azimuthal and vertical directions are labeled by local Cartesian coordinates x, y and z. The origin of the frame follows an unperturbed fluid element moving in a circular orbit. The radial logarithmic derivative of Ω is

$$A = \frac{1}{2}\frac{\mathrm{d}\Omega}{\mathrm{d}\ln R}|_{x=0}$$

and characterises the local shear.

The fundamental dynamical equations in this rotating frame are the mass continuity equation,

$$\frac{\partial \rho}{\partial t} + \boldsymbol{\nabla}\cdot(\rho\boldsymbol{v}) = 0, \tag{1}$$

where ρ is the mass density of the gas and $\boldsymbol{v}$ is its velocity, and the Navier-Stokes equation with a kinematic viscosity ν_V,

$$\frac{\partial \boldsymbol{v}}{\partial t} + (\boldsymbol{v}\cdot\boldsymbol{\nabla})\boldsymbol{v} + 2\Omega\hat{\boldsymbol{z}}\times\boldsymbol{v} + \boldsymbol{\nabla}(2A\Omega x^2) + \frac{1}{\rho}\boldsymbol{\nabla}(p + \frac{B^2}{2}) - \frac{1}{\rho}(\boldsymbol{B}\cdot\boldsymbol{\nabla})\boldsymbol{B} = \frac{1}{\rho}\boldsymbol{\nabla}\cdot(\rho\nu_V\boldsymbol{\sigma}) \tag{2}$$

where p is the thermal pressure, $\boldsymbol{B}$ is the magnetic field (divided by $2\sqrt{\pi}$) and $\sigma_{ij} = \frac{1}{2}(\partial_i v_j + \partial_j v_i) - \frac{1}{3}\partial_k v_k \delta_{ij}$ is the stress tensor. The vertical gravity is neglected. The induction equation is

$$\frac{\partial \boldsymbol{B}}{\partial t} = \boldsymbol{\nabla}\times(\boldsymbol{v}\times\boldsymbol{B} - \eta_B\boldsymbol{J}) \tag{3}$$

where $\boldsymbol{J} \equiv \boldsymbol{\nabla}\times\boldsymbol{B}$ and η_B is the resistivity. Finally, we adopt an ideal gas equation of state with adiabatic index γ so that the internal energy equation reads

$$\frac{p}{\gamma-1}\frac{\mathrm{D}\ln(p\rho^{-\gamma})}{\mathrm{D}t} = \eta_B J^2 + \rho\nu_V\boldsymbol{\sigma}\boldsymbol{:}\boldsymbol{\nabla}\boldsymbol{v} - \Lambda \tag{4}$$

where Λ is the net cooling function.

Equations (1) to (4) form the governing system of which we seek particular solutions.

2.2   Incompressible vertical modes

We seek solutions that are a single Fourier mode with vertical wavenumber k and a constant vertical magnetic field $\boldsymbol{B}_0$ superimposed on the background shear. The solutions have the form

$$\boldsymbol{v} = 2Ax\hat{\boldsymbol{y}} + \boldsymbol{u} \quad \boldsymbol{B} = B_0\hat{\boldsymbol{z}} + \boldsymbol{b} \tag{5}$$

with

$$\boldsymbol{u} = \delta\boldsymbol{u}\, e^{st+ikz} \quad \boldsymbol{b} = \delta\boldsymbol{b}\, e^{st+ikz} \tag{6}$$

We assume $\delta\boldsymbol{u} \perp \hat{\boldsymbol{z}}$ and $\delta\boldsymbol{b} \perp \hat{\boldsymbol{z}}$. It is understood that the physical solutions are obtained by taking the real part of equations (5). (In particular, note that the δ amplitudes may be complex.)

For this form of solution, the mass continuity equation states that the Lagrangian derivative of ρ is zero, hence the density remains constant along the trajectories of the fluid elements. Thus, ρ is constant in time and space *provided* that it was uniform initially, which we shall assume.

We further assume that the pressure p is initially a function of z only. This property is also conserved in time for our particular flow. Upon substitution of equations (5) and (6) into equation (2), we obtain

$$s\boldsymbol{u} + 2Au_x\hat{\boldsymbol{y}} + 2\boldsymbol{\Omega} \times \boldsymbol{u} + \frac{1}{\rho}\hat{\boldsymbol{z}}\,\partial_z\left(p + \frac{(\Re[\boldsymbol{b}])^2}{2}\right) - \frac{1}{\rho}B_0ik\boldsymbol{b} = -\nu_V k^2\boldsymbol{u} \tag{7}$$

where we assume that ν_V is uniform and we use the symbols $\Re[z]$ and $\Im[z]$ to denote the real and imaginary parts of a complex number z. Note that this equation makes sense only if the $\hat{\boldsymbol{z}}$ pressure gradient terms vanish, a key point to which we shall return below.

Finally, assuming a uniform resistivity η_B, the induction equation becomes

$$s\boldsymbol{b} - 2Ab_x\hat{\boldsymbol{y}} - B_0ik\boldsymbol{u} = -\eta_B k^2\boldsymbol{b} \tag{8}$$

In what follows, we shall use the new variables

$$\nu = k^2\nu_V$$

and

$$\eta = k^2\eta_B.$$

The only remaining non-linear term in the above equations is the total pressure gradient $\partial_z p_{\text{tot}}$ with $p_{\text{tot}} = p + (\Re[\boldsymbol{b}])^2/2$. It is also the only term of this equation with a z component. If, for the moment, we assume that this term is zero, then the problem for $\boldsymbol{u}$ and $\boldsymbol{b}$ is contained within equations (7) and (8) and decouples from the energy equation. We are left with a simple linear, incompressible problem with viscosity and resistivity, which we now turn to solve.

The linear Euler equation may be written

$$\mathbb{E}\boldsymbol{u} = \frac{B_0ik}{\rho}\boldsymbol{b} \tag{9}$$

with the 2×2 matrix $\mathbb{E}$ defined by

$$\mathbb{E} = \begin{bmatrix} s + \nu & -2\Omega \\ 2(\Omega + A) & s + \nu \end{bmatrix} \tag{10}$$

where we considered only the x and y components of the vectors. The induction equation can be rewritten similarly

$$\mathbb{F}\boldsymbol{b} = B_0ik\boldsymbol{u} \tag{11}$$

with

$$\mathbb{F} = \begin{bmatrix} s + \eta & 0 \\ -2A & s + \eta \end{bmatrix}. \tag{12}$$

Operating on equation (11) with $\mathbb{E}$ and using equation (9) produces the linear eigenvalue problem

$$(\mathbb{E}\mathbb{F} + k^2v_A^2\mathbb{I})\boldsymbol{b} = 0, \tag{13}$$

where $\mathbb{I}$ is the identity matrix and $k^2v_A^2 = B_0^2k^2/\rho$ where v_A is the Alfvén speed. s is therefore a root of the determinant (det) polynomial

$$P_{\nu,\eta}(s) = \det[\mathbb{E}\mathbb{F} + k^2v_A^2\mathbb{I}],$$

which is precisely the MRI dispersion relation.

We need compute directly only the restricted case $P_{0,\eta}(s)$ for $\nu = 0$ since the full linear problem with parameters (s, ν, η) is equivalent to the one with $(s + \nu, 0, \eta - \nu)$. Hence, $P_{\nu,\eta}(s) = P_{0,\eta-\nu}(s + \nu)$:

$$P_{0,\eta}(s) = (\eta + s)^2(\kappa^2 + s^2) + 2\left[2A\Omega + s(s + \eta)\right]k^2v_A^2 + (kv_A)^4 = 0 \tag{14}$$

and in developed form

$$P_{0,\eta}(s) = s^4 + 2\eta s^3 + (\eta^2 + 2k^2v_A^2 + \kappa^2)s^2 + 2\eta(k^2v_A^2 + \kappa^2)s + \kappa^2\eta^2 + 4A\Omega k^2v_A^2 + (kv_A)^4 \tag{15}$$

with $\kappa^2 = 4\Omega(A + \Omega)$ which is identical to the form given by equation (12) in Fleming et al. (2000). The general dispersion relation may then be obtained by replacing s by $s + \nu$ and η by $\eta - \nu$ in equation (14):

$$P_{\nu,\eta}(s) = (\eta + s)^2\left[\kappa^2 + (\nu + s)^2\right] + 2\left[2A\Omega + (s + \nu)(s + \eta)\right]k^2v_A^2 + (kv_A)^4 = 0 \tag{16}$$

2.3   Condition for a homogeneous total pressure

For the solutions whose form is of the previous section, the internal energy equation becomes

$$\frac{\partial p}{\partial t} = (\gamma - 1)\left[\eta(\Im[\boldsymbol{b}])^2 + \rho\nu(\Im[\boldsymbol{u}])^2 - \Lambda\right]. \tag{17}$$

Note that the $\boldsymbol{v}\cdot\boldsymbol{\nabla}p$ term vanishes because $\boldsymbol{v}$ has components only along $\hat{\boldsymbol{x}}$ and $\hat{\boldsymbol{y}}$ whereas $\boldsymbol{\nabla}p$ is along $\hat{\boldsymbol{z}}$. The above may be rewritten as an equation for the total gas plus magnetic pressure:

$$\frac{\partial}{\partial t}\left(p + \frac{(\Re[\boldsymbol{b}])^2}{2}\right) = \Re[s\boldsymbol{b}]\cdot\Re[\boldsymbol{b}] + (\gamma - 1)(\eta(\Im[\boldsymbol{b}])^2 + \rho\nu(\Im[\boldsymbol{u}])^2 - \Lambda). \tag{18}$$

From here on, we restrict the cooling function to be of the form $\Lambda = -\Gamma + \alpha p$ with Γ and α constant. Since ρ is a constant, this is equivalent to taking Λ to be a linear function of temperature. (In effect, this is just the leading Taylor series expansion of $\Lambda(T)$ around an arbitrary point in temperature.) The effect of Γ may be absorbed into p_{tot} by adding a linear function of time with no spatial dependence, and without loss of generality, we may set $\Gamma = 0$. We rewrite the time evolution equation for the total pressure accordingly:

$$\frac{\partial p_{\text{tot}}}{\partial t} + (\gamma - 1)\alpha p_{\text{tot}} = \Re[s\boldsymbol{b}]\cdot\Re[\boldsymbol{b}] + (\gamma - 1)(\eta(\Im[\boldsymbol{b}])^2 + \rho\nu(\Im[\boldsymbol{u}])^2 + \frac{\alpha}{2}\Re[\boldsymbol{b}]\cdot\Re[\boldsymbol{b}]). \tag{19}$$

The right hand side of equation (19) must be independent of position for a self-consistent solution. Formally, these terms may be expressed as a spatially constant term plus a term of the form $\Re[a\exp(2st + 2ikz)]$, with the complex amplitude a constant in both time and space:

$$a = \left[s - (\gamma - 1)(\eta - \frac{\alpha}{2})\right]\frac{\delta b_x^2 + \delta b_y^2}{2} - (\gamma - 1)\nu\rho\frac{\delta u_x^2 + \delta u_y^2}{2} \tag{20}$$

where we remind the reader that δb_x, δb_y, δu_x and δu_y are complex numbers. Our task, therefore, is to investigate the conditions under which a vanishes. If this can be done, the full set of equations is reduced to the linear problem of the previous section plus equation (19), which now reads

$$\frac{\partial p_{\text{tot}}}{\partial t} + (\gamma - 1)\alpha p_{\text{tot}} = \left[\Re[s] + (\gamma - 1)(\eta + \frac{\alpha}{2})\right]\frac{|\delta b_x|^2 + |\delta b_y|^2}{2} + (\gamma - 1)\nu\rho\frac{|\delta u_x|^2 + |\delta u_y|^2}{2} \tag{21}$$

where $|Z|^2 = (\Re[Z])^2 + (\Im[Z])^2$ (modulus). When the solution of the linear problem (7)-(8) (without the total pressure gradient) is inserted into this last equation, one gets a simple solution for p_{tot} of the form :

$$p_{\text{tot}}(t) = p_1\exp(2\Re[s]t) + p_2\exp(-(\gamma - 1)\alpha t) \tag{22}$$

with

$$p_1 = \frac{1}{(\gamma - 1)\alpha + 2\Re[s]}\left\{\left[\Re[s] + (\gamma - 1)(\eta + \frac{\alpha}{2})\right]\frac{|\delta b_x|^2 + |\delta b_y|^2}{2} + (\gamma - 1)\nu\rho\frac{|\delta u_x|^2 + |\delta u_y|^2}{2}\right\} \tag{23}$$

and

$$p_2 = p_{\text{tot}}(0) - p_1. \tag{24}$$

The above is a solution of the non-linear problem if and only if the total pressure gradient term vanishes, hence if and only if $a = 0$. In the case with shear, this condition can be recast in the form of a fifth order polynomial $Q(s) = 0$. To see this, we first express the components of $\delta\boldsymbol{b}$ and $\delta\boldsymbol{u}$ in terms of δb_x only. The first row of equation (13) gives δb_y as a function of δb_x:

$$f \equiv \frac{\delta b_y}{\delta b_x} = \frac{(s + \nu)(s + \eta) + 4A\Omega + k^2v_A^2}{2\Omega(s + \eta)} \tag{25}$$

Note this is valid only provided that Ω is non-zero. If $\Omega = A = 0$, then δb_x and δb_y are independent (see the case without shear in section 4 below).

Equation (11) now allows us to express $\delta\boldsymbol{u}$ in terms of $\delta\boldsymbol{b}$ and hence δb_x:

$$\delta u_x = \frac{1}{ikB_0}(s + \eta)\delta b_x \tag{26}$$

and

$$\delta u_y = \frac{1}{ikB_0}\left[-2A + (s + \eta)f\right]\delta b_x. \tag{27}$$

a can now be rewritten

$$a = \delta b_x^2\left[s - (\gamma - 1)(\eta - \frac{\alpha}{2})\right]\frac{1}{2}(1 + f^2) + \delta b_x^2(\gamma - 1)\nu\frac{1}{2k^2v_A^2}\left[(s + \eta)^2 + (-2A + (s + \eta)f)^2\right]. \tag{28}$$

Finally we substitute f thanks to equation (25) and gather quantities over the same denominator:

$$a = \frac{\gamma - 1}{2} \frac{Q(s)}{(s + \eta)^2} \delta b_x{}^2 \tag{29}$$

where $Q(s)$ is the following polynomial in s:

$$Q(s) = \left(\frac{1}{\gamma - 1} s - \eta + \frac{\alpha}{2} \right) \left[(s + \eta)^2 + \frac{1}{4\Omega^2} \left((s + \nu)(s + \eta) + 4A\Omega + k^2 v_A^2 \right)^2 \right]$$

$$+ \frac{\nu}{k^2 v_A^2} (s + \eta)^2 \left[(s + \eta)^2 + \frac{1}{4\Omega^2} \left((s + \nu)(s + \eta) + k^2 v_A^2 \right)^2 \right]. \tag{30}$$

The homogeneity condition $a = 0$ is therefore satisfied if s is a root of Q. Henceforth, we refer to Q as the homogeneity polynomial. Note that it is generally of order 5.

The parameters of the system are hence Ω and A for the shear, kv_A (which actually combines B_0, k and ρ) for the magnetic field, ν, η, γ and α (or Λ) for the properties of the gas. For a given set of these parameters, we now want to find a growth rate s which satisfies the dispersion relation (16) and for which the total pressure gradient vanishes, ie: $P(s) = 0$ and $Q(s) = 0$.

We shall first restrict our analysis to real roots s in simple cases, although we treat the case with no shear exhaustively (see section 4) . Most of the solutions presented are therefore standing wave solutions, except in the case without shear. There we find circularly polarised waves and other propagating disturbances.

3   INVISCID SOLUTIONS

In this section we set $\nu = 0$. The homogeneity polynomial becomes

$$Q(s) = \left(\frac{1}{\gamma - 1} s - \eta + \frac{\alpha}{2} \right) \left[(s + \eta)^2 + \frac{1}{4\Omega^2} \left(s^2 + \eta s + 4A\Omega + k^2 v_A^2 \right)^2 \right]. \tag{31}$$

We choose to find a common *real* root to P and Q. The only way Q can have a real root is if $s = (\gamma - 1)(\eta + \frac{\alpha}{2})$ because the quantity in the square brackets of expression (31) is strictly positive for s real.

3.1   Cooling/heating

The extra degree of freedom granted by the presence of thermal losses/gains makes such solutions easier to find: given a real root s of P (ie: a standing mode), we need only adjust α to

$$\alpha = 2(\eta - \frac{1}{\gamma - 1} s). \tag{32}$$

The final solution is then simply given by the expressions (5), (6) and (22).

3.2 $\alpha = 0$

From (32) with $\alpha = 0$ we immediately see that $s = (\gamma - 1)\eta$ is required for a uniform total pressure. Using this in the relation $P(s) = 0$, we obtain a quadratic equation for η^2:

$$\gamma^2 (\gamma - 1)^2 \eta^4 + 2\gamma[(\gamma - 1)k^2 v_A^2 + 2\Omega\gamma(\Omega + A)]\eta^2 + k^2 v_A^2 (4A\Omega + k^2 v_A^2) = 0 \tag{33}$$

Alternatively, this can also be viewed as a quadratic equation for $k^2 v_A^2$:

$$(kv_A)^4 + [4A\Omega + 2(\gamma - 1)\gamma\eta^2]k^2 v_A^2 + \gamma^2 \eta^2 [4\Omega(A + \Omega) + (\gamma - 1)^2 \eta^2] = 0. \tag{34}$$

Either of these equations allows a determination of the set of parameters (η, kv_A) for which there exists a solution. For example, in the case where $\kappa^2 = 4\Omega(\Omega + A) > 0$, equation (34) has a real root for $k^2 v_A^2$ provided that

$$\eta^2 < \frac{\Omega A^2}{\gamma(A + \gamma\Omega)} \tag{35}$$

which sets an upper limit on the resistivity. The request that this root be positive sets up the additional constraint

$$\eta^2 < \frac{-2A\Omega}{\gamma(\gamma - 1)} \tag{36}$$

which forces $A > 0$ and sets an additional upper limit on the resistivity. The final condition (an upper limit on resistivity) is

$$\eta^2 < \frac{-A\Omega}{\gamma} \min\left(\frac{2}{\gamma - 1}, \frac{-A}{A + \gamma\Omega} \right). \tag{37}$$

3.3 $\eta = \nu = 0$, adiabatic

In this case, the condition (34) simply becomes $kv_A = 2\sqrt{-A\Omega}$, so $A < 0$ for such a solution to exist. The growth rate is then $s = 0$, a marginally stable mode of the MRI. The dispersion relation has only real roots, $s = 0$ (double root) and $s = \pm 2\sqrt{\Omega(\Omega - A)}$, but the growing and decaying modes do not fulfill the homogeneity condition. (As mentioned above, this solution is also valid when the constant Γ is non zero, which is not, strictly speaking, adiabatic.)

4   NON ROTATING FLOW

Here we set $A = \Omega = 0$ and drop the assumption that s is real. Without rotation and shear, $\hat{\boldsymbol{x}}$ is no longer a special direction; the direction $\hat{\boldsymbol{z}}$ is still defined by the mean field $\boldsymbol{B}_0$. The system is now invariant under rotation of axis $\hat{\boldsymbol{z}}$ and the eigenvectors of the linear system now depend on two independent variables, say δb_x and δb_y. The effective dispersion relation becomes:

$$P(s) = R(s)^2 = 0 \tag{38}$$

with

$$R(s) = (s + \eta)(s + \nu) + k^2 v_A^2. \tag{39}$$

Without shear, the homogeneity condition $a = 0$ with the definition (20) becomes

$$\frac{a}{\gamma - 1} = \left[\frac{\alpha}{2} - \eta + \frac{s}{\gamma - 1} + \frac{\nu}{k^2 v_A^2}(s + \eta)^2 \right] \frac{\delta b_x^2 + \delta b_y^2}{2} = 0 \tag{40}$$

This can be achieved if either $\delta b_x^2 + \delta b_y^2 = 0$, or if the factor inside the brackets vanishes.

4.1   Torsional Alfvén waves

In this case, we simply set $\delta b_x^2 + \delta b_y^2 = 0$ by choosing either of the circularly polarised cases $\delta b_x = \pm i \delta b_y$. Now, both roots s of the dispersion relation $R = 0$ provide a possible solution:

$$s_\pm = -\frac{\eta + \nu}{2} \pm \sqrt{\left(\frac{\eta - \nu}{2}\right)^2 - k^2 v_A^2} \tag{41}$$

When $kv_A < |\eta - \nu|/2$ we get two standing modes. When $kv_A > |\eta - \nu|/2$, $s_\pm$ have imaginary parts and the two solutions correspond to right or left circularly polarized waves. In particular, when $\alpha = \nu = \eta = 0$, we recover circularly polarised torsional Alfvén waves which are indeed well-known solutions of their non-linear governing equations.

4.2   Non polarised waves without shear

If $\delta b_x^2 + \delta b_y^2$ is non zero, then we need to find the common roots of P and the simple quadratic

$$Q(s) = \frac{\alpha}{2} - \eta + \frac{s}{\gamma - 1} + \frac{\nu}{k^2 v_A^2}(s + \eta)^2 \tag{42}$$

which is the factor inside the brackets of equation (40). Since $P = R^2$, to find a common root of P and Q means to find a common root of Q and R. For simplicity we assume $\gamma = 5/3$, but it is not much more difficult to do without this assumption.

We detail our analysis of the common roots of P and R in appendices A for complex roots and B for real roots. Here, we simply summarise our result that $\alpha > \sqrt{6}|kv_A|$ is a necessary and sufficient condition for the existence of common complex roots, i.e. : the existence of propagating disturbances as solutions. We are also able to give an expression for kv_A in terms of the other parameters of the problem in the case when there exist a common real root, i.e. : when a standing wave is solution of the problem.

5   SOLUTIONS WITH SHEAR, RESISTIVITY, VISCOSITY AND COOLING

In general, one may not be interested in the complete range of parameters for which a solution exists. A benchmark calculation only needs one set of parameters. In that case, we may simply pick a growth rate and treat $P = 0$ and $Q = 0$ as equations for $k^2 v_A^2$ (both quadratic). Then the process of finding a set of parameters that yields a solution is greatly simplified. As an illustration, we set $\Omega = 1$, $A = -3/2$, $\nu = 1/5$ and $\eta = 1/10$ and seek $k^2 v_A^2$ and α as functions of s. $P = 0$ implies

$$k^2 v_A^2 = \frac{1}{50}\left(74 - 5s(3 + 10s) \pm 5\sqrt{218 - 10s(11 + 40s)}\right). \tag{43}$$

Then the equation $Q = 0$ is linear in the variable α. For example, if we now seek a standing wave solution with the growth rate $s = 1/2$, we find

$$k^2 v_A^2 = \frac{54 + 15\sqrt{7}}{50} \simeq 1.874 \tag{44}$$

and from $Q(1/2) = 0$

$$\alpha = -\frac{899569 + 13560\sqrt{7}}{597490} \simeq -1.566. \tag{45}$$

Here we have an example of an explicit benchmark with viscosity, resistivity and heating in a shearing box.

6 NUMERICAL BENCHMARKS

The original Zeus3D code (see Stone & Norman 1992a,b) is not written in a fully conservative form. In particular, equation (4) is used to compute the evolution of internal energy. In general, this scheme leads to significant loss of total energy. For example, if discretisation errors lead to kinetic or magnetic energy losses, this artificial dissipation is not reflected in viscous heating or Ohmic heating and the total energy decreases. This energy is effectively "radiated" away.

However, when viscous and/or resistive terms are included in the code, part or all of the total energy loss is recovered as heat and the total energy loss is reduced. As an illustration, we ran torsional Alfvén tests with the original Zeus3D code, and with a total energy conserving scheme (see below). Fig. 1a shows that the total energy scheme performs much better in a case without explicit resistive and viscous terms: the internal energy scheme heavily distorts the wave profile (this was already noted by Turner et al. 2003). On the other hand, fig. 1b shows that the internal energy scheme with some resistivity and viscosity is indistinguishable from the total energy scheme. Because of the finite resolution (32 zones) there is still some numerical dissipation and the numerical results are slightly damped compared to the analytical solution. The difference between the analytical solution and the actual simulations disappears on the scale of these graphs at a resolution of 128 zones for both these tests.

In principle, grid based schemes cannot avoid numerical dissipation. However, it is possible to make numerical dissipation look more like physical dissipation by using a conservative form for the evolution equations. For example, we can evolve the total energy, and deduce the internal energy as the remainder of the mechanical (kinetic, magnetic plus potential) energy subtracted from the total energy. In this case, we write the total energy equation as:

$$\frac{\partial \mathcal{E}}{\partial t} + \boldsymbol{\nabla} \cdot \boldsymbol{\mathcal{F}} = -\Lambda \tag{46}$$

with

$$\mathcal{E} = e + \frac{1}{2}\rho v^2 + \frac{1}{2}b^2 + \rho\Phi \tag{47}$$

where $\Phi = 2A\Omega x^2$ is the tidal potential energy, e is the internal energy and the total energy flux is

$$\boldsymbol{\mathcal{F}} = \boldsymbol{v}\left(p + e + \frac{1}{2}\rho v^2 + \rho\Phi\right) + (\boldsymbol{B}\times\boldsymbol{v})\times\boldsymbol{B} + \eta_B \boldsymbol{J}\times\boldsymbol{B} - \rho\nu_V \boldsymbol{\sigma}\cdot\boldsymbol{v}. \tag{48}$$

We have implemented this in the Zeus3D code. This is similar to the work of Turner et al. (2003) and Hirose et al. (2006), but we also include Ohmic stresses $\eta_B \boldsymbol{J}\times\boldsymbol{B}$ and tidal potential energy flux $\boldsymbol{v}\rho\Phi$. The question arises at what stage of the calculation each term of the total energy flux $\boldsymbol{\mathcal{F}}$ should be evaluated. We ran various benchmarks (torsional Alfvén waves and standing mode solutions presented in the previous sections) and varied the order with which the fluxes were computed. We noted that it is crucial to compute each flux term simultaneously with its corresponding source or transport term. In particular, it is critical to compute $(\boldsymbol{B}\times\boldsymbol{v})\times\boldsymbol{B}$ using the time centred values for $\boldsymbol{B}$ and $\boldsymbol{v}$ computed with the method of characteristics (MOC, see Stone & Norman 1992b). On the other hand, the kinetic energy flux should not be directionally split the way the momentum transport step is.

Finally, it is much better to join the tidal flux to the density transport term and not to the tidal force source term. We now illustrate how we used our analytical solutions to prove this last point (see fig. 2). We used our code with two slightly different versions in order to reproduce the analytical solution presented in section 5. The first version (dotted lines on fig. 2) would compute the tidal potential flux $\rho\Phi\boldsymbol{v}$ at the same time as the tidal source term. The second version (dashed lines on fig. 2) would compute this flux jointly with the transport step. In the first version, the resulting total pressure gradient is not flat and the magnetic energy loses its low z/high z symmetry. The second version retains the correct symmetry and displays a flat pressure profile. Note however that in both computations the average total pressure and the magnetic pressure are slightly lower than the analytical solution. Both simulations shown are for cubic boxes of 32 zones aside and higher resolution improves the magnetic pressure more efficiently than the total pressure.

The final scheme we adopted was to compute $\boldsymbol{\mathcal{F}}$ in five distinct steps:
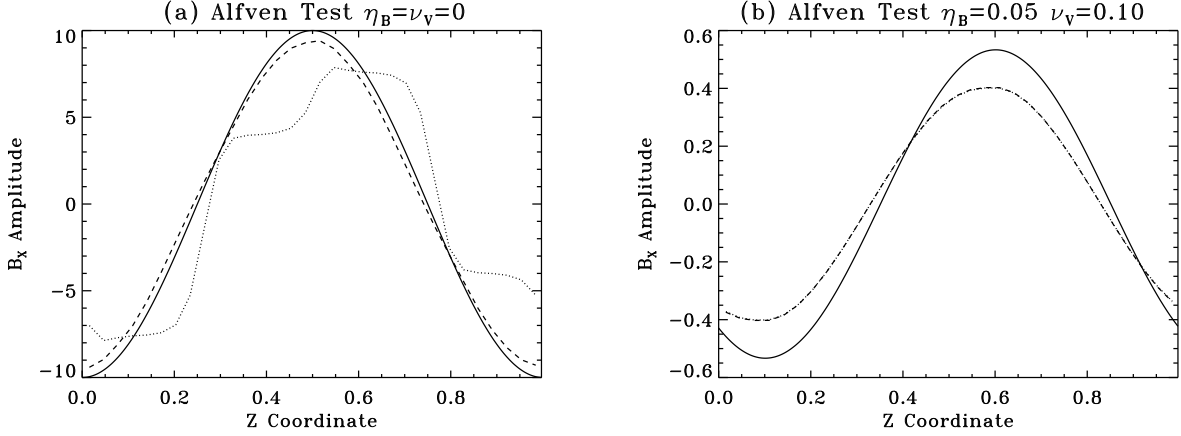
Figure 1. Torsional Aflvén waves tests. *Solid line:* analytical solution, *dotted line:* internal energy scheme, *dashed line:* total energy scheme. Parameters are $\Omega = A = \alpha = 0$, $\gamma = 5/3$, $B_0 = \delta b_x = 10$, $k = 2\pi$. The simulation box is a cube of 32 zones aside and has physical length 1. The plots show snapshots of the azimuthal magnetic field evaluated on a vertical line. *(a) Left panel:* $\nu_V = \eta_B = 0$, after 3 oscillations. *(b) Right panel:* $\nu_V = 0.1$ and $\eta_B = 0.05$ at a time correponding to 9.9 oscillations.
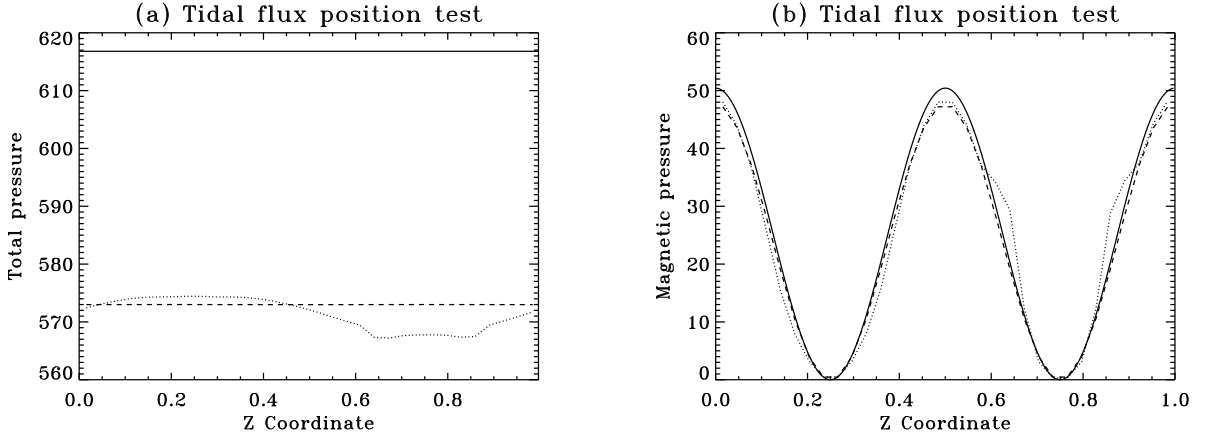
Figure 2. A benchmark with shear, resistivity, viscosity and heating (see section 5). The wave number is $k = 2\pi$ and $\rho = 1$. We display the total pressure (a, left panel) and the magnetic pressure $(b_x^2 + b_y^2)/2$ (b, right panel). The time is $t = 6$ which corresponds to 12 e-folding times ($s = 1/2$). The *solid line* is the analytical solution, the *dashed line* is for a total energy scheme where the flux of tidal potential $\rho\Phi\boldsymbol{v}$ is computed jointly with the transport step and the *dotted line* is a total energy scheme where this flux is computed with the tidal source term.

- $\boldsymbol{v}p$ is first computed using an upwinded pressure computed at the same time as the pressure gradient source,
- the viscous term is computed at the same time as the viscous forces,
- the remainder of the flux $\boldsymbol{v}\left(e + \frac{1}{2}\rho v^2 + \rho\Phi\right)$ is added after the hydrodynamical transport term,
- the resistive term is computed along with the resistive electromotive force,
- the $(\boldsymbol{B}\times\boldsymbol{v})\times\boldsymbol{B}$ term is finally computed with the MOC advanced $\boldsymbol{v}$ and $\boldsymbol{B}$ which are used for the constrained transport of $\boldsymbol{B}$.

Along this process, we evolve the internal energy e thanks to equation (4). In particular, this provides an advanced estimate for e in the flux term $\boldsymbol{v}(e + \ldots)$. At the end of these steps, we compute $\mathcal{E}^*$ with the updated values of all variables. We then use equation (46) with $\Lambda = 0$ to advance the total energy to its new value $\mathcal{E}$. If the internal energy scheme was perfect, we would have $\mathcal{E}^* = \mathcal{E}$. However, this is almost never the case and a correction $\mathcal{E} - \mathcal{E}^*$ needs to be applied to e in order to conserve total energy. We deduce the rate of correction of internal energy $\dot{e} = (\mathcal{E} - \mathcal{E}^*)/\sqcup$ where Δt is the length of the time step. The internal energy is finally updated with $\Lambda \neq 0$ and $\dot{e}$ thanks to an isochore heating/cooling step.

7   NUMERICAL VISCOSITY AND RESISTIVITY

In appendix C, we present a method to estimate the numerical resistivity and viscosity in a code. The idea is to probe the numerical dissipation in the absence of explicit resistivity and viscosity, and to determine the effective numerical dissipation coefficients by fitting results to our analytical solutions that include viscosity and resistivity. In the following, we write for short η_N and ν_N for the numerical resistivity and viscosity. As explained in the appendix C, we measure directly $(\eta_N + \nu_N)k^2$ and $(\eta_N - \nu_N)k^2$ respectively to second and first order in $(\eta_N - \nu_N)k/v_A$. We then deduce the values for η_N and ν_N. We used this method mainly on the internal energy scheme version of the Zeus3D code since it is the version that is generally used in published applications.

7.1   General trends

Our method provides a direct estimate for the numerical dissipation in a code. Therefore it gives the numerical floor for the physical viscosity and resistivity in a given code. For codes devoid of a viscous or resistive term, it also allows to compute the effective Reynolds and Prandtl numbers. We now investigate general trends of the numerical dissipation.

We first examine wave numbers along the vertical direction. In figure 3, we examine the dependence of η_N and ν_N with various parameters. The Courant number (or Courant coefficient) is a parameter that controls the time step of a code. In the Zeus3D code it is defined as

$$C = \frac{\Delta t}{\Delta x} \max \left(\sqrt{v^2 + c^2 + v_A^2} \right) \tag{49}$$

where v, c and v_A are the local speed, sound speed and Alfvén speed in the fluid, Δx is the size of a zone, Δt is the size of a time step and the maximum is taken over all grid zones. We measured the dependence on resolution, wave number, perturbation amplitude and mean field amplitude for three different Courant numbers: 0.01, 0.1 and 0.5. we display the results only for a Courant number of 0.1 and we discuss the differences when applicable. We first ran a standard run with parameters $\beta = 2/B_0^2 = 400$, $k = 2\pi$, an amplitude of $|\delta b_x| = 0.001$, $\rho = 1$, a Courant coefficient of $C = 0.1$ and a spatial resolution of 32 zones in all three directions (hence $\Delta x = 1/32$ since we use a physical length of 1 for the size of the box). We then varied each parameter in turn away from these values.

Figure 3a and 3b show that η_N and ν_N scale linearly with the size of the time step and as the square of the size of a grid cell. An interpretation of these trends is that our scheme is 1st order in time but 2nd order in space. Note that at a Courant coefficient of 0.5, the numerical η_N changes sign. As a whole, the numerical scheme remains stable in the sense that $\eta_N + \nu_N$ is always positive. However, η_N or ν_N individually could be negative. $\eta_N < 0$ indicates that the MHD part of the time step behaves like antidiffusion. Antidiffusivity in Zeus was already noted by Falle (2002) who also pointed out that lower Courant numbers lower antidiffusion. More recently, Fromang & Papaloizou (2007) also pointed out antidiffusion in Zeus at large scales. Here, we quantify the effect in more detail. The wave number with the lowest numerical resistivity turns out to be $\boldsymbol{k} = 2\pi(\hat{\boldsymbol{x}} + \hat{\boldsymbol{y}} + \hat{\boldsymbol{z}})$. The resistivity of this mode is negative for all Courant coefficients above 0.12 (see dashed line on figure 3b). Such negative values for the resistivity are only found for wave numbers with coordinates lower or equal than 2: only the largest scales are affected. With the Zeus3D code, it might nevertheless be safer to adopt Courant coefficients below 0.5 or to include some minimal amount of physical resistivity in the code. Including physical dissipation has the advantage that it will also improve the energy budget, as noted in the previous section.

In figure (3b) it appears that the dissipation has a finite limit as the time step tends toward zero. Indeed, the finite space resolution does not allow the scheme to achieve an infinite precision. Similarly, in figure (3a) the scaling of the numerical dissipation is a power of -2 in the number of zones at low space resolution, but at high space resolution it turns into a shallower power of -1. Indeed, the Courant number is kept fixed (hence $\Delta t/\Delta x$ is fixed) and the scheme is second order in space but only first order in time: at high resolution, the numerical dissipation is dominated by the order of the time integration scheme. At a higher Courant number of 0.5, the shallower slope of -1 occurs at even lower space resolution. At a Courant number of 0.01, the slope of -2 is seen over the whole range of space resolution we tested. Note that the numerical resistivity also turns out to be negative for the highest resolutions at Courant numbers 0.1 and 0.5.

Figure 3c shows the dependence of η_N and ν_N on the wave number. Unlike a physical viscosity or resistivity, η_N and ν_N vary according to the length scale, with a maximum at $k = 8 \times 2\pi\hat{\boldsymbol{z}}$ (four grid points inside each wavelength). There is no clear scaling but figure 3c suggests that the total dissipation behaves roughly like a power with an exponent between 1 and 2 (1.6 seems to be the best match) until it reaches the maximum dissipation. The quantity $(\eta_N - \nu_N)k/v_A$ can be as high as 0.5 for $k = 8 \times 2\pi\hat{\boldsymbol{z}}$, so the method of appendix C is not accurate for higher wave numbers.

Our estimates show that numerical dissipation is nearly independent of the amplitude of the initial perturbation (although there is a slight dependence on it at a Courant number of 0.5). However, we observe a strong dependence on the amplitude of the mean magnetic field (see figure 3d). The numerical viscosity appears to be directly proportional to the mean magnetic field at low Courant number (0.01) with some additional dissipation at low β for higher Courant numbers. The numerical resistivity obeys the same law, with an additional change of sign at low values of β (note: it remains positive at low β for a Courant
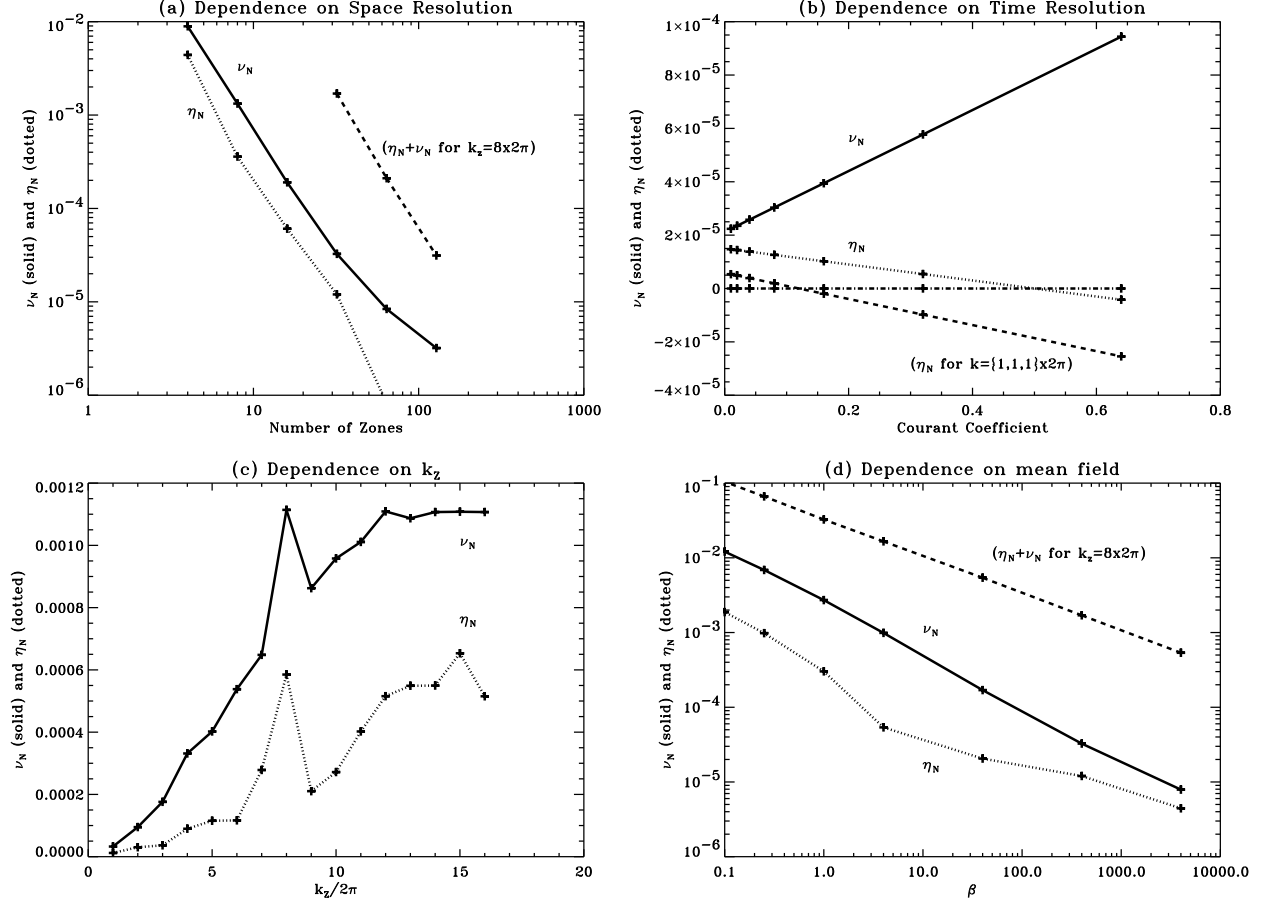
Figure 3. We plot the numerical viscosity ν_{N} (solid) and resistivity η_{N} (dotted) vs various parameters such as (a) total zone number (the dashed line is $\eta_{\mathrm{N}} + \nu_{\mathrm{N}}$ for $\boldsymbol{k} = 2\pi \times 8\hat{\boldsymbol{z}}$), (b) Courant coefficient (see Stone & Norman 1992a,b)(the dashed line is η_{N} for the wave vector $\boldsymbol{k} = 2\pi(\hat{\boldsymbol{x}} + \hat{\boldsymbol{y}} + \hat{\boldsymbol{z}})$ and the dash-dotted line indicates the zero threshold.), (c) k_z for a mode with $\boldsymbol{k}$ along $\hat{\boldsymbol{z}}$ and (d) amplitude of the mean field (the dashed line is $\eta_{\mathrm{N}} + \nu_{\mathrm{N}}$ for $\boldsymbol{k} = 2\pi \times 8\hat{\boldsymbol{z}}$)

number of 0.01). This explains why the benchmarks of the previous section (which are for large mean field amplitudes) have strong dissipation compared to the standard runs of the present section. This might be an issue for the computation of the saturated state of the MRI with Zeus3D. If numerical dissipation does increase with the turbulent magnetic energy, this could affect the total effective dissipation in the system.

    To summarise these results, we suggest to approximate the total numerical dissipation with the following scaling formula:

$$\eta_{\mathrm{N}} + \nu_{\mathrm{N}} \simeq 0.76 \Delta x^2 \beta^{-\frac{1}{2}} \left(\frac{k}{2\pi} \right)^{1.6} + 1.08 \Delta x C \beta^{-1}. \tag{50}$$

We calibrated both coefficients of this formula on figure 3b and the exponents for Δx, C, k and β are obtained from figures 3a, 3b, 3c and 3d respectively. Formula (50) should therefore be taken only as indicative for values of parameters not too far from those tested here. Furthermore, as stated, the scaling in k should also be taken with caution (see figure 3c).

7.2 Anisotropy

Our method allows us to quantify the anisotropy of the numerical dissipation. We measured the numerical dissipation for all wave vectors in the Fourier domain of the box with coordinates of the form $k_i = 2\pi n$ with $i = x, y, z$ and $0 \leqslant n \leqslant 16$ (a grid of $17^3 - 1$ measurements). Many shearing box simulations actually use half the resolution in the azimuthal y direction compared to the radial x and vertical z directions. We therefore did the same measurements (with $k_y \leqslant 8 \times 2\pi$) on a cubic box with 32x16x32 zones in which the grid cells have an aspect ratio 1:2:1.

In figure 4a we plot all $\eta_N + \nu_N$ measurements for the 32^3 (cubic cells) simulation against the norm of the wave vector. The overall shape of this diagram roughly follows figure 3c with a maximum of dissipation at $15\times2\pi$. Even for cubic grid cells, the numerical dissipation already shows some degree of anisotropy: at a given wave number it varies widely. We detail the distribution of this spread in figure 5a for wavenumbers k which have $2\pi N_k \leqslant k < 2\pi(N_k + 1)$ with $N_k = 15$. Wave vectors with the highest dissipation are those that point towards a cartesian axis. For a fixed $|k|$, wave vectors along an axis maximise the size of a single component. We therefore suggest that the numerical dissipation at a given wave vector is dominated by the dissipation at its maximum coordinate. For wave vectors of norm $|k|$ higher than 16, the three coordinates have similar values, hence the numerical dissipation is more and more isotropic. Interestingly, the numerical Prandtl number

$$Pm_N = \nu_N/\eta_N$$

is quite isotropic for all wave numbers and slightly decreases from 2 at small wave numbers to 1 at large wave numbers (see figure 4c; the very small wave numbers have higher Prandtl numbers, but the numerical dissipation is much lower there). The isotropy of the Prandtl number is even better at lower Courant coefficients ($C = 0.01$), with a mean value closer to (slightly above) 1 and a spread between 1 and 2. It is interesting to compare these results to the recent work of Fromang et al. (2007) who estimate Prandtl numbers between 2 and 4 for Zeus. It is also striking that all our measured Prandtl numbers are greater than 1.

As mentioned, a few directions yield a negative resistivity. The corresponding wave vectors at $C = 0.5$ have their coordinates amongst the following list: (1,1,1), (1,1,0), (2,1,1), (2,2,1), (2,2,2) and their permutations.

For elongated cells, the diagram 4b is only slightly more complicated. It is similar to figure 4a, but replicates its pattern extended by a factor 2 in amplitude and squeezed by a factor 2 in wave numbers. This additional feature results from the halved resolution in the y direction. As shown on figure 5b, the dissipation is not symmetric to x-y exchange. On the contrary, y wave vectors undergo much larger dissipation. This shows up even more at smaller wave numbers as seen in figure 5c and 5d. However, the Prandtl number does not show more anisotropy than in the case of a cubic cell: numerical resistivity and viscosity react in the same way to the resolution loss in the y direction.

7.3   Scheme

We tested our code in various configurations to investigate the impact on numerical dissipation. We found that isothermal simulations are slightly less dissipative than adiabatic simulations (with numerical resistivity more negative in general). We could hardly see any difference between the internal and the total energy schemes. We also found that to use the non-linear artificial resistivity as coded in Stone & Norman (1992a) did not change the numerical dissipation: our tests did not trigger significant artificial viscosity because of the incompressible nature of our test flows.

8   DISCUSSION

8.1   Incompressibility

We discuss here a few caveats, limitations and possible extensions of our method. First, we wish to stress that the condition of incompressibility on the modes is a crucial one. Indeed, any change in density will alter the $1/\rho$ factor in the Euler equation, introducing additional non-linearities that might be difficult to address with analytical tools.

In section 7 we have measured an equivalent numerical viscosity for *torsional Alfvén waves* only. This gives a first estimate of the numerical dissipation, but an arbitrary MHD flow cannot be decomposed into such modes. For example we cannot probe any viscosity associated to compressible flows (see section 7.3). On the other hand, the viscosity of compressible flows could be measured by studying the width of shock fronts, or with damped magnetosonic waves in the linear regime.

8.2   Boundary conditions

Periodic boundary conditions in z are essential for our analysis. For example, reflective boundary conditions will mix two Fourier modes which very likely will open the way for a cascade at many other wave numbers.

It should be noted that our analytic shear solutions do not strongly test the implementation of shearing box boundary conditions. Indeed, except for the mean steady flow, our solutions for non-zero Ω depend *only* on the z coordinate. For example, these benchmarks could not tell if the code uses periodic boundary conditions in the x direction or shearing box boundary conditions.
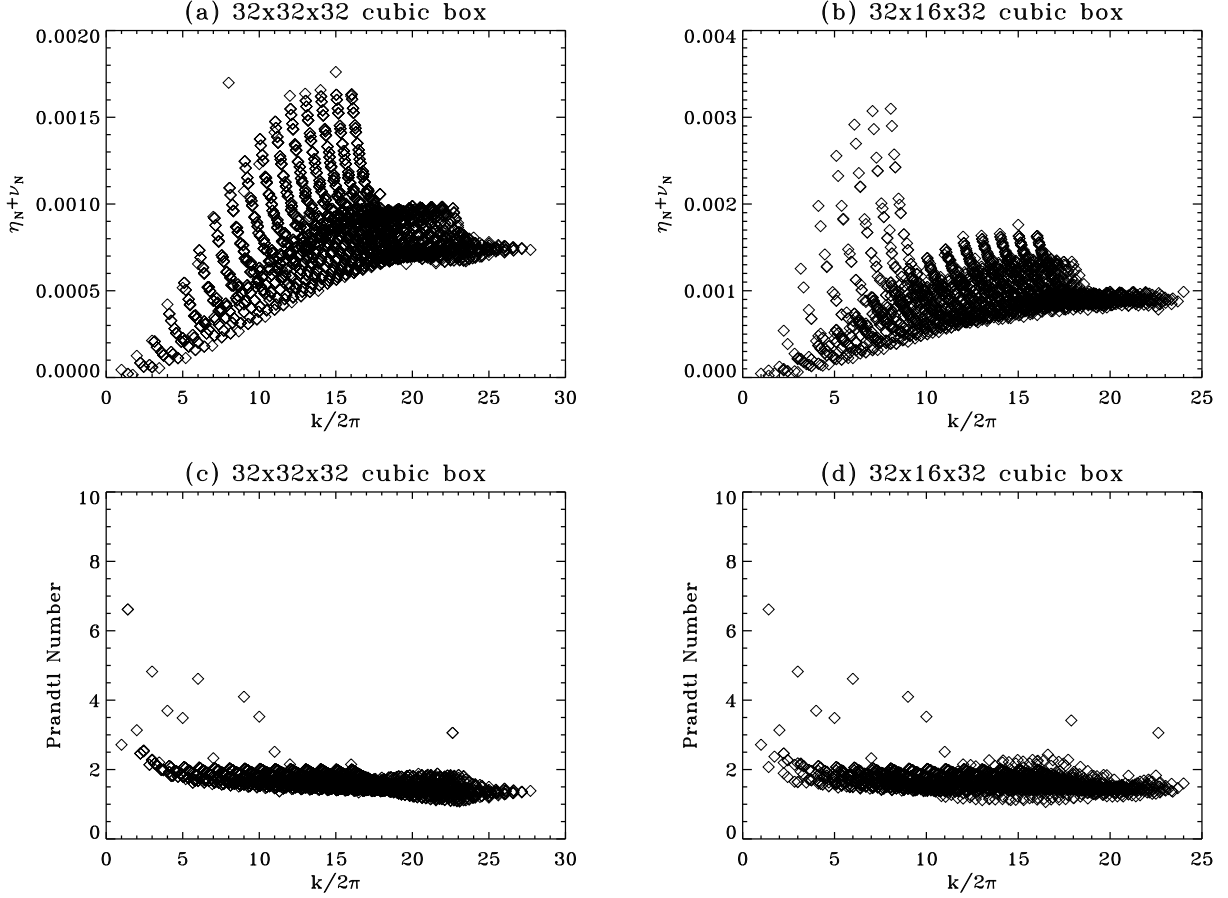
Figure 4. We show the total numerical dissipation $\eta_N + \nu_N$ (panels a and b, upper side) and numerical Prandtl number $Pm_N = \nu_N/\eta_N$ (panels c and d, lower side) vs. k for every wavevector of the computational box. Panels a and c (left hand side) are for a 32x32x32 zones computational box. Panels b and d (right hand side) are for a 32x16x32 zones box with elongated cells.

To improve this, we could need to find solutions with spatial variation in more than one direction. A non-zero k_x is in fact perfectly tractable, and the equations hardly change if one uses the expression $(\boldsymbol{k}.\boldsymbol{B_0})^2/\rho = k_z^2 B_0^2/\rho$ instead of $k^2 v_A^2$. However, it will not probe more efficiently the shearing box boundary conditions: periodicity in x would still be indistinguishable from shearing box conditions for most variables.

In order to probe the shearing box boundary conditions, a non-zero azimuthal wave number is needed. Unfortunately, a non-zero k_y yields an Eulerian wave vector changing in time (Balbus & Hawley 1992). In that case, the homogeneity condition changes in time and the total pressure gradient cannot be dealt with at all times. However, it is worth noting that the total pressure term is still in this case the only non-linear term. Semi-analytic solutions of the equations without the pressure term can be found for MHD shearing waves. We plan in future work to benchmark the MHD shearing box boundary conditions by using such equations.

8.3 Thermal diffusion

A thermal diffusion coefficient can very easily be included in our analytical solutions. Under the assumption of a uniform density, the thermal diffusion term in equation (19) is proportional to

$$\chi \triangle p = \chi \triangle \left(p_{\text{tot}} - \frac{1}{2} \Re[\boldsymbol{b}] \cdot \Re[\boldsymbol{b}] \right) = \chi 2 k^2 \Re[\boldsymbol{b}] \cdot \Re[\boldsymbol{b}] \tag{51}$$

where χ is the uniform thermal diffusion coefficient. We recall that the term due to cooling in equation (19) is $\alpha/2 \, \Re[\boldsymbol{b}] \cdot \Re[\boldsymbol{b}]$. To include thermal diffusion in our formalism is hence equivalent to use $\alpha + 4k^2\chi$ in place of α.
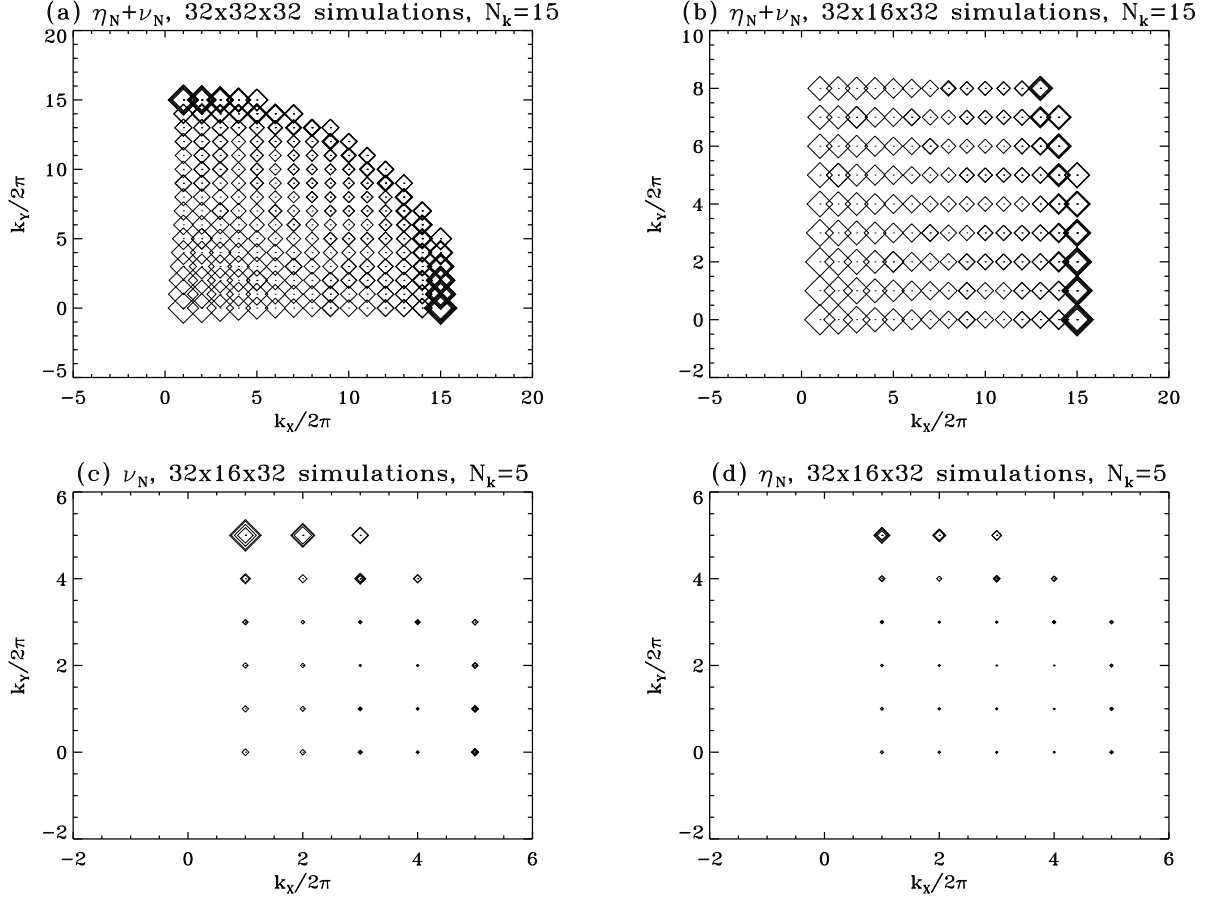
Figure 5. We show the total numerical dissipation $\eta_N + \nu_N$ (panels a and b, upper side) and numerical resistivity ν_N (panels c and d, lower side) for each wave number with positive coordinates and such that $2\pi N_k \leqslant k < 2\pi(N_k + 1)$. The size of the symbols codes for the magnitude of the quantity plotted and their position marks their x and y coordinates. Results for wave vectors with same x and y coordinates but differing z coordinates are overplotted on top of each other. Panels (a) and (b) compare the simulations with cubic cells (a) to the simulation with elongated cells (b) in the case where N_k=15. Panels (c) and (d) compare numerical viscosity (c) and resistivity (d) in the case with elongated grid cells for $N_k = 5$.

8.4   Total pressure gradient

The assumption of a homogeneous total pressure is the cornerstone of our analysis. This requirement might not be as strong as it seems at first glance. Indeed, the gradient of total pressure in the Euler equations naturally drives MHD flows towards a state of uniform total pressure. As a result, our solutions should be close approximations to the exact MHD flows even in cases when the condition of homogeneity is not met, provided that the real flow remains at a nearly constant density.

9   CONCLUSIONS

This paper consists of variations on a theme: the channel solution. We have extended previously known analytical solutions to more general and more physical cases, including viscosity, resistivity and cooling. We also showed the connection between torsional Alfvén waves and channel solutions.

We used these solutions to calibrate the implementation of a conservative scheme in Zeus3D. We also measured the numerical resistivity and viscosity of torsional Alfvén waves in Zeus3D. In particular, we showed that lower time steps should be used in Zeus3D in order to guarantee a positive resistivity when no physical resistivity is used. We would rather recommend to use a minimal amount of physical resistivity. It also is best to use isotropic resolution since the numerical dissipation is more anisotropic for elongated cells. Finally we find a dependence of the numerical dissipation on the amplitude of the magnetic field.

Although in this paper we stressed the numerical applications of these solutions, they are of interest in their own right. In particular, we have established a stronger basis for understanding the stability analysis of channel solutions: it should

now be possible to compute parasitic instabilities with improved microphysics. As a result, we hope to better understand the saturation properties of MRI turbulence.

APPENDIX A: PROPAGATING DISTURBANCES WITH ZERO SHEAR

We work here in the framework and notations of section 4.2. We first assume that there exists a common complex root s to R and Q. Then its complex conjugate $\bar{s}$ also is a common root. Being only second degree, R and Q have the same roots s and $\bar{s}$. Hence they differ only by a real proportionality constant, and the remainder R_1 of the Euclidian division of R by Q needs to be identically zero:

$$R_1(s) = a_1 s + a_0 \tag{A1}$$

with

$$a_1 = \nu - \eta - \frac{3}{2} \frac{k^2 v_A^2}{\nu} \tag{A2}$$

and

$$a_0 = (\nu - \eta)\eta + k^2 v_A^2 \left(1 + \frac{-\alpha + 2\eta}{2\nu}\right). \tag{A3}$$

Both coefficients a_0 and a_1 must vanish if R and Q are to have a common complex root. This puts two constraints on the three remaining parameters η, ν and kv_A so that η and ν can be expressed in terms of kv_A. Setting a_1 equal to zero, we get

$$\eta = \nu - \frac{3k^2 v_A^2}{2\nu}. \tag{A4}$$

We now use this expression into the equation $a_0 = 0$ which yields a quadratic equation for ν:

$$14\nu^2 - 2k^2 v_A^2 \alpha \nu + 15 k^2 v_A^2 = 0 \tag{A5}$$

which has only one real positive root

$$\nu = \frac{1}{14} \left(\alpha + \sqrt{\alpha^2 + 210 k^2 v_A^2}\right). \tag{A6}$$

Equation (A4) now provides the value for η

$$\eta = \frac{1}{35} \left(6\alpha - \sqrt{\alpha^2 + 210 k^2 v_A^2}\right) \tag{A7}$$

which is positive for $\alpha > \sqrt{6}|kv_A|$.

In order to get a common complex root to P and Q, the resistivity and viscosity need hence to be determined by expressions (A7) and (A6). Using these expressions for η and ν in the dispersion relation $R(s) = 0$ provides the two actual growth rates s and $\bar{s}$ as

$$s_\pm = \frac{-17\alpha - 3\sqrt{\alpha^2 + 210 k^2 v_A^2}}{140} \pm i\sqrt{r} \tag{A8}$$

with

$$r = 95 k^2 v_A^2 + \alpha \sqrt{\alpha^2 + 210 k^2 v_A^2} - \alpha^2. \tag{A9}$$

The corresponding solutions are therefore propagating disturbances (i.e. they have a non zero imaginary part) only when $r > 0$ which is equivalent to setting the condition $\alpha > -\frac{19}{4}|kv_A|$. Since we already required the more stringent condition $\alpha > \sqrt{6}|kv_A|$ in order to get $\eta > 0$, physically plausible solutions exist only when $\alpha > \sqrt{6}|kv_A|$ for propagating disturbances.

APPENDIX B: STANDING WAVES WITH ZERO SHEAR

We work here in the framework and notations of section 4.2. We now assume that s is a real common root to P and R. In that case, $R_1(s) = 0$ immediately gives s in terms of the parameters of the other problem:

$$s = \frac{-2\nu\eta(\nu - \eta) + \alpha k^2 v_A^2 - 2(\eta + \nu)k^2 v_A^2}{2\nu(\nu - \eta) - 3k^2 v_A^2} \tag{B1}$$

Using s in P or Q, we finally arrive at a relational constraint for the defining of the problem. As an explicit example, $k^2 v_A^2$ can be expressed in terms of α, η and ν:

$$k^2 v_A^2 = \frac{1}{18}\left[-\alpha^2 + 7\alpha(\eta + \nu) + 2\nu^2 - 41\eta\nu - 10\eta^2 + (-\alpha + 2\nu + 5\eta)\sqrt{\alpha^2 - \alpha(10\nu + 4\eta) + \nu^2 + 44\eta\nu + 4\eta^2}\right]. \tag{B2}$$

APPENDIX C: A METHOD TO MEASURE NUMERICAL RESISTIVITY AND VISCOSITY

In section 4.1 we showed that circularly polarised waves with nonzero viscosity or resistivity are solution of the non-linear equations. In principle, if we start our simulation with one of the eigenmodes corresponding to the growth rate $s_\pm = \pm i w$ (equation 41 for $\eta = \nu = 0$), we should obtain the time evolution of a torsional Alfvén wave as a result of the computation.

However, the finite grid and time stepping resolution introduce some numerical defects. For example, figures 1a and 1b show that numerical results undergo some dissipation. In these figures, the dashed line corresponds to a wave with a slightly lower amplitude than a pure torsional Alfvén wave after three oscillation periods. This suggests that the numerical errors in the code may behave like an equivalent viscosity and resistivity. In principle we could define their effective values if we were able to fit a model evolution to the actual numerical output of the code.

In this appendix, we are motivated to compute the evolution of a system which starts with the initial conditions for a torsional Alfvén wave (with $\eta = \nu = 0$), but which is evolved with some amount of viscosity ν_N and resistivity η_N. Recall that $\eta = k^2 \eta_N$ and $\nu = k^2 \nu_N$ where η_N and ν_N are the effective resistivity and viscosity. We present the results to first order in $(\eta - \nu)/kv_A = (\eta_N - \nu_N)k/v_A$.

We choose the initial phase such that $\delta b_x = 1$. The initial conditions for a torsional Alfvén wave give $\delta u_x = 1$ and $\delta b_y = \delta u_y = i$.

We first assume that the code preserves well the initial uniform density profile[1]. According to section 4.1 there exist only two incompressible modes that can be excited with growth rates given by equation (41). We decompose our initial conditions on the two corresponding eigenmodes which have $\delta u_{x\pm} = (s_\pm + \eta)/(ikv_A)\,\delta b_{x\pm}$:

$$\delta u_x = 1 = \alpha_+ \frac{s_+ + \eta}{iw} + \alpha_- \frac{s_- + \eta}{iw} \tag{C1}$$

and

$$\delta b_x = 1 = \alpha_+ + \alpha_- \tag{C2}$$

with

$$\frac{s_\pm + \eta}{ikv_A} \simeq \frac{\eta - \nu}{2ikv_A} \pm 1 \tag{C3}$$

and where α_+ and α_- are the complex weights of the two eigen modes.

We solve for α_+ and α_- and retain the first order in $(\eta - \nu)/kv_A$:

$$\alpha_+ = \frac{1}{2}\left(1 + \frac{kv_A + i\frac{\eta - \nu}{2}}{\sqrt{k^2 v_A^2 - \left(\frac{\eta - \nu}{2}\right)^2}}\right) \simeq 1 + i\frac{\eta - \nu}{4kv_A} \tag{C4}$$

and

$$\alpha_- = 1 - \alpha_+ \simeq -i\frac{\eta - \nu}{4kv_A}. \tag{C5}$$

The non-linear coupling between these two modes can only occur through the total pressure gradient term and it happens that this term vanishes to first order in $(\eta - \nu)/kv_A$. The temporal evolution of the system can hence be approximated by its linear evolution

$$\delta u_x = \alpha_+ \frac{s_+ + \eta}{ikv_A} \exp(s_+ t) + \alpha_- \frac{s_- + \eta}{ikv_A} \exp(s_- t) \tag{C6}$$

and

---

[1] We actually checked that to enforce $\rho = 1$ in the code did not change much the measured ν and η.
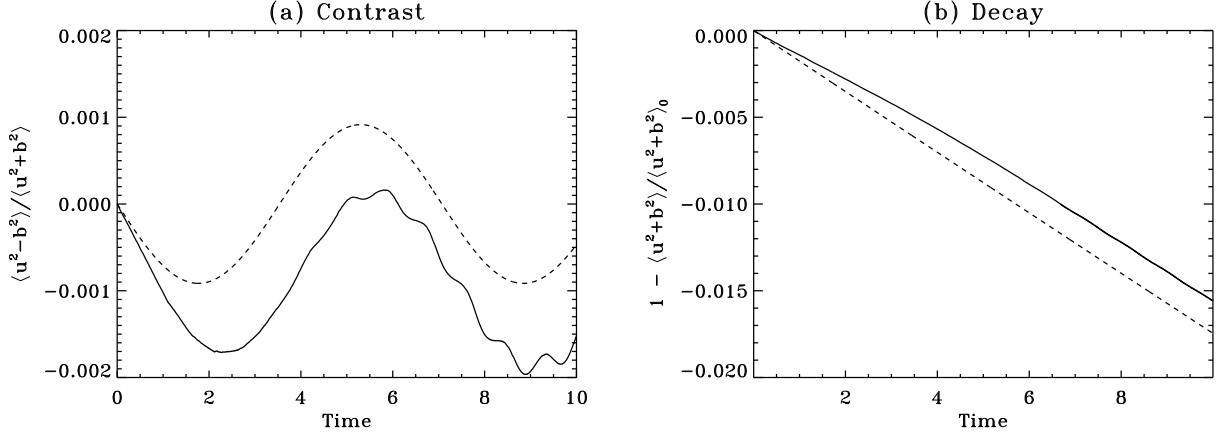
Figure C1. On the *left panel* (a) we display (solid line) the evolution of the contrast $< (\Re[\boldsymbol{u}])^2 - (\Re[\boldsymbol{b}])^2 > / < (\Re[\boldsymbol{u}])^2 + (\Re[\boldsymbol{b}])^2 >$ in our standard run as well as (dashed line) the result of equation (C11) where $\eta - \nu$ is determined from the first time step of the simulation. On the *right panel* (b) we display (solid line) the evolution of the quantity $1 - < (\Re[\boldsymbol{u}])^2 + (\Re[\boldsymbol{b}])^2 > / < 2\cos^2(\boldsymbol{k.r}) >$ in our standard run as well as (dashed line) the result of equation (C10) where $\eta + \nu$ is determined from the first time step of the simulation.

$$\delta b_x = \alpha_+ \exp(s_+ t) + \alpha_- \exp(s_- t). \tag{C7}$$

We finally recover the temporal evolution of the perturbed quantities as

$$\Re[u_x] = \exp\left(-\frac{\eta + \nu}{2} t\right) \left[\cos(k v_A t + \boldsymbol{k.r}) + \frac{\eta - \nu}{2 k v_A} \sin(k v_A t) \cos(\boldsymbol{k.r}) \right] \tag{C8}$$

and

$$\Re[b_x] = \exp\left(-\frac{\eta + \nu}{2} t\right) \left[\cos(k v_A t + \boldsymbol{k.r}) - \frac{\eta - \nu}{2 k v_A} \sin(k v_A t) \cos(\boldsymbol{k.r}) \right]. \tag{C9}$$

The y component of these fields can be recovered because of the circular polarisation conditions $b_y = i b_x$ and $u_y = i u_x$. We choose to recover η and ν from their sum and difference through the volumic averages of kinetic and magnetic energy:

$$\frac{1}{2} < (\Re[\boldsymbol{u}])^2 + (\Re[\boldsymbol{b}])^2 >= \exp\left(-(\eta + \nu) t\right) < \cos^2(\boldsymbol{k.r}) > \tag{C10}$$

and

$$< (\Re[\boldsymbol{u}])^2 - (\Re[\boldsymbol{b}])^2 >= (\eta - \nu) \frac{\sin(2 k v_A t)}{2 k v_A} < (\Re[\boldsymbol{u}])^2 + (\Re[\boldsymbol{b}])^2 > . \tag{C11}$$

Hence, we find the total dissipation $\eta + \nu$ from the exponential decay of the kinetic plus magnetic energy. And we get the difference $\eta - \nu$ from the relative difference between these two forms of energy. Note that these final expressions yield $\eta + \nu$ with one more order of accuracy in $(\eta - \nu)/k v_A$ than $\eta - \nu$. We checked a posteriori that $(\eta - \nu)/k v_A$ is indeed small for all measurements performed in this paper except for the highest wave numbers (see section 7.1).

In order to save computing time, we evaluate η and ν on the very first time step of the simulation. Figures C1a and C1b show that this provides reasonable estimates for equations (C11) and (C10). The match is in fact perfect only for the first few time steps. The later discrepancy between our model for the code diffusion and the actual results of the code is probably due to the dispersive properties of the scheme which we do not take into account. This discrepancy actually narrows down at higher Courant numbers which are known to be less dispersive. However, figure C1 shows that our model captures the bulk of the numerical artifacts.

Finally, in order to ensure that the initial fields have zero divergence, we convert real wave numbers k to discrete wave numbers $k' = 2\sin(k\Delta x/2)/\Delta x$ when we compute the relations between the amplitudes of the fields. Δx is the size of a pixel in the units of the computation.

REFERENCES

Balbus S. A., Hawley J. F., 1991, ApJ, 376, 214
—, 1992, ApJ, 400, 610
Falle S. A. E. G., 2002, ApJ Letter, 577, L123
Fleming T. P., Stone J. M., Hawley J. F., 2000, ApJ, 530, 464

Fromang S., Papaloizou J., 2007, ArXiv e-prints, 7053621

Fromang S., Papaloizou J., Lesur G., Heinemann T., 2007, ArXiv e-prints, 7053622

Goodman J., Xu G., 1994, ApJ, 432, 213

Hawley J. F., Balbus S. A., 1992, ApJ, 400, 595

Hill G. W., 1878, Am. J. math., 1, 5

Hirose S., Krolik J. H., Stone J. M., 2006, ApJ, 640, 901

Stone J. M., Norman M. L., 1992a, ApJS, 80, 753

—, 1992b, ApJS, 80, 791

Turner N. J., Stone J. M., Krolik J. H., Sano T., 2003, ApJ, 593, 992